RA

RSCPublishing

ARTICLE

Cite this: DOI: 10.1039/x0xx00000x

Received 00th January 2012,
Accepted 00th January 2012

DOI: 10.1039/x0xx00000x

www.rsc.org/

Tungstite nanoparticles prepared by microwave-assisted synthesis and their application as a hole transporting layer in organic solar cells

Clément Bottois[a,b,c], Konstantin Tarasov[b†], Olivier Poncelet[b], Régis Pecquet[c], Noëlla Lemaitre[a].

Thin films of tungstite ($WO_3{\cdot}H_2O$) nanoparticles have been used as a hole transporting layer (HTL) in organic solar cells and demonstrated good performances. The nanoparticles were synthesized by dissolving WCl_6 in benzyl alcohol and using a microwave-assisted heating at 130°C and ambient pressure. The obtained nanoparticles exhibit a platelet form whose lateral size can be tuned from 30 nm to 250 nm by modifying the metallic salt concentration in solution. These particles were dispersed in an ethanol solution allowing the formation of homogeneous thin films with a relatively low roughness and a suitable work function (5.0 eV). The films were tested as a hole transporting layer in polymer solar cells in a standard structure with P3HT:PCBM as the active layer. A good V_{OC} has been observed due to a suitable energy level alignment and an average power conversion efficiency of 3.2% has been achieved with a best PCE of 3.49%. Moreover, an annealing treatment was not required to obtain a good photovoltaic performance (PCE = 3.1%). This represents a gain in cost and time in the device fabrication compared to post-deposition treated films obtained by the sol-gel method.

1 Introduction

Recently, power conversion efficiencies above 10% have been achieved for organic photovoltaic devices[1]. However, if gaining efficiency is still catching the spotlights, the stability remains an important issue to be improved in order to see a large development of this technology. Poly(3,4-ethylene dioxythiophene): polystyrene sulfonic acid (PEDOT:PSS) is a well-known *p*-type semiconducting polymer, which is largely used as a hole transporting layer (HTL) in organic solar cells. However, due to its acidic and hygroscopic properties, it has been identified as a cause of rapid ageing [2]. For this reason, inorganic materials, believed to be more stable, are of interest to replace PEDOT:PSS. Transition metal oxides (TMO) are mostly considered for this purpose, with the use of chromium[3], molybdenum[4–6], nickel[7,8], tungsten[9–12] and vanadium[13,14] oxides. In addition, hydrated oxides such as hydrate vanadium pentoxide ($V_2O_5{\cdot}0.5H_2O$)[15] and hydrogen bronzes[16,17] (H_xMoO_3 and $H_xV_2O_5$) have also been tested as HTL films and showed good results. If first reports described deposition techniques in vacuum, such as sputtering[3], pulsed-laser deposition[7] or thermal evaporation[9,12], non-vacuum methods, particularly, the solution processed deposition, have emerged[5,6,8,10,11,13,14] with the prospect of being applied in industrial processes such as roll-to-roll processing. The sol-gel method allows the formation of films with thicknesses below 10 nm, but usually needs a relatively high annealing temperature (up to 250 °C) and a long conversion time[8,10,14] to completely evaporate and decompose organic residues. Another solution processed method uses a colloidal dispersion of nanoparticles with a subsequent deposition to form thin layers. In this case, a post-deposition treatment is not required as the material is already formed.

Among the mentioned above TMOs, tungsten oxide attracts attention for its low toxicity and suitable opto-electrical properties. The application of the solution-based approach for HTL has already been demonstrated through sol-gel processes[10,18,19]. Also, the nanoparticle approach has been explored by *Stubhan et al.*[11] employing a commercial solution of WO_3 particles synthetized by a flame spray pyrolysis method[20].

Developing solution methods can be a major advantage to obtain a simple and quick access to nanoparticles. A way to

---

[a] *Univ. Grenoble Alpes, INES, F-73375, Le Bourget du Lac, France. CEA Grenoble, LITEN, Department of Solar Technologies, F-73375, Le Bourget du Lac, France.*

[b] *CEA Grenoble, LITEN, Nanomaterials Technologies Department, F-38054 Grenoble Cedex 9, France.*

[c] *PCAS Longjumeau, 91160 Longjumeau, France.*

† Corresponding author, email: konstantin.tarasov@cea.fr

DOI: 10.1039/b000000x/

synthesize tungsten oxide nanoparticles via a solution-based method is to use tungsten hexachloride (WCl_6) as a precursor and benzyl alcohol (BnOH) as a solvent. This solvothermal synthesis firstly described by *Niederberger et al* in 2002 [21] leads to hydrous tungsten oxide (tungstite, $WO_3 \cdot H_2O$). This synthesis has also been realized with microwave heating[22] and nanoparticle sizes below 10 nm have been obtained. To our knowledge, the use of tungstite nanoparticles as a hole transporting layer has not been studied yet.

In this study, a low temperature (130°C) synthesis of tungstite nanoparticles has been performed using WCl_6 and benzyl alcohol heated by microwave irradiation. The influence of the metal salt concentration on the nanoparticle size has been investigated. The nanoparticles dispersed in ethanol and deposited as thin films were further used as a hole transporting layer in organic bulk heterojunction (BHJ) solar cells with poly-3-hexylthiophene (P3HT) as the donor material and [6,6]-phenyl-C_{61}-butyric acid methyl ester ($PC_{60}BM$) as the acceptor. This tungstite incorporating devices were compared to cells using PEDOT:PSS as the HTL. The influence of the thermal treatment of the inorganic HTL on the performances has been investigated.

2 Experimental section

2.2 Synthesis

Tungsten hexachloride (WCl_6, ≥ 99.9% trace metal basis) and anhydrous benzyl alcohol (BnOH, 99.8%) were purchased from Sigma-Aldrich, stored and weighed in a glove-box under inert atmosphere (N_2) and controlled H_2O pressure (<1 ppm). Absolute ethanol used for washing was purchased from Carlo Erba reagents. Products were used as received without further purification.

In a glass vial, a given amount of WCl_6 (0.25, 0.50, 1.0 or 1.5 g) was dissolved in 25 mL of BnOH, leading to a concentration in metallic salt of 0.025, 0.050, 0.10 or 0.15 mol/L, respectively. The sample was stirred for 15 minutes. Then, the solution was heated up to 130°C by microwave irradiation using a Sairem Miniflow 200SS apparatus at a frequency of 2.45 GHz and a maximum power of 200 W. The temperature inside the vial was recorded using an optical-fiber probe protected by a thin glass tube. The experiments were carried out at ambient pressure. The maximum temperature was reached within 80 seconds, while the total heating-time was 20 minutes. Then, the sample was left to cool down at room temperature and was centrifuged. The supernatant was removed and the powder was re-dispersed by ultrasound in absolute ethanol. This washing procedure was repeated three times. Finally, the particles were dispersed in an ethanol (EtOH) solution where a small amount of water was added ($EtOH/H_2O$ 99.5/0.5 by volume). For each sample, the final concentration of tungstite in the solution was 2.5 wt %.

2.2 Nanoparticles and thin film characterization

Nanoparticles morphology and size were characterized using a scanning electron microscope (SEM) Hitachi S-4100 operating at 30 kV. As the particles are not spherical, the measured sizes correspond to the longest particle dimension. The average value was calculated from at least one hundred particle size measurements. The TEM image was obtained using a Tecnai OSIRIS microscope operating at 200 kV. X-ray diffraction patterns (XRD) were recorded on powders using a D8 Bruker X-ray diffractometer and the CuK_α radiation. Thermal analysis (TG-DSC) was performed using a Setaram instrument LabSys Evo with a sample mass of 50 mg at a heating rate of 5°C/min under an argon flow. The hydrodynamic diameters (D_{hyd}) and size distribution in colloidal solution were obtained by the dynamic light scattering method (DLS) using a Malvern Zetasizer Nano-ZS apparatus. The same apparatus was used to determine the zeta potential of the solution.

Kelvin probe force microscopy (KPFM) and atomic force microscopy (AFM) experiments were carried out on a Bruker Dimension ICON microscope with Nanoscope IIIa electronics and performed in a MBraun glove-box with a controlled pressure in O_2 and H_2O. PtIr coated silicon tips (Budget Sensors) with first resonant frequency in the 60–90 kHz range and force constant of 3 $N.m^{-1}$ were used. Tapping^{TM} mode was applied for the morphology measurements allowing the evaluation of the roughness root mean square (R_{RMS}) values. The reference samples for work function determination were made of ruthenium and aluminum. The film thickness was measured with a stylus-based surface profilometer (KLA-TencorAlphaStapIQ) at a scan rate of 50 $\mu m.s^{-1}$. At least 10 measures were made on different testing samples (different samples for one condition and several measures at random places on each sample).

2.3 Device fabrication and photovoltaic measurements

Organic solar cells were fabricated on a pre-etched glass/ITO substrate. It was pre-cleaned by a UV-ozone treatment for 30 min in air. Hole Transporting Layer (HTL) was spin-coated using either PEDOT:PSS (Baytron-P) annealed for 30 min at 180°C in air or a solution of tungstite nanoparticles synthesized in the present study.

The bulk heterojunction active layer (AL – 200 nm) was fabricated from a P3HT:$PC_{60}BM$ solution in anhydrous 1,2-dichlorobenzene (99%, from Sigma-Aldrich) (concentration in P3HT : 26 g/L ; ratio donor/acceptor 1:0.6 in weight; annealed for 10 min at 140°C under N_2). P3HT and $PC_{60}BM$ were purchased from Merck. A 10 nm TiO_x electron transporting layer (ETL) was formed from a nanoparticles solution[23] and annealed for 10 min at 120°C in a glove-box. Those three layers (HTL, AL and ETL) were prepared by spin-coating. Finally, a cathode of aluminum (200 nm thickness) was evaporated at 10^{-5} mbar through a shadow mask. This leads to solar cells with an active surface of 28 mm^2. The whole cell is illustrated in Figure 1. Photovoltaic measurements were carried out under inert atmosphere using AM 1.5, 100 mW/cm^2 illumination, obtained by an Oriel SP94043A (Xe Lamp) Solar simulator. Characteristics and power conversion efficiencies were measured via a computer controlled Keithley SMU 2400 unit. A monocrystalline silicon solar cell, calibrated at the

Fraunhofer Institut Solare Energiesysteme (Freiburg, Germany), was used as a reference cell to confirm stabilization of the 100 mW/cm^2 illumination. The used apparatus was a standard system that is widely used and gives mismatch factors of around 5% in the 300 to 1100 nm range in comparison with AM1.5G. The mismatch factors were measured using a spectrophotometer AECUSOFT, Flashspec. The shunt (R_{sh}) and serie (R_s) resistance were calculated from the current-voltage characteristics at – 1 V and 1 V, respectively.

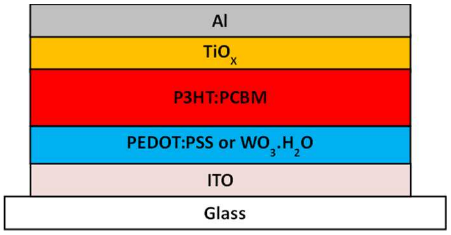

Figure 1. Scheme of the organic solar cell in the standard structure with studied HTL.

3 Results and discussion

3.1 Nanoparticle synthesis

The synthesis conditions used in the present work (T< 145°C and concentration of WCl_6 < 0.25 mol/L) were relatively mild and were chosen to ensure the formation of tungstite rather than other tungsten oxides[22]. The dissolution of WCl_6 in benzyl alcohol is accompanied by a change in the solution color from red to blue within a few seconds. This is likely due to the replacement of some chlorides by alkoxy and hydroxyl-groups as ligands[24]. After heating, the colloid color becomes green-blue indicating a formation of tungstite particles.

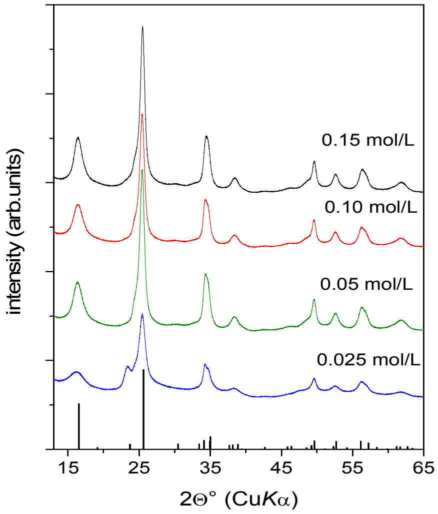

Figure 2. XRD patterns of nanoparticles synthesized at different concentrations in comparison with the reference pattern of tungstite $WO_3 \cdot H_2O$ (grey bars, JCPDS # 043-0679).

The preparation of homogeneous and ultrathin (<50 nm) nanoparticle films requires a severe control of particle size. In view of this, the effect of the precursor salt concentration on the particle size was studied in detail. XRD patterns of the nanoparticles synthetized in solutions with the salt concentrations varying from 0.025 to 0.15 mol/L are shown in Figure 2. The X-ray powder profiles of all the obtained products can be attributed to $WO_3 \cdot H_2O$ (orthorhombic structure), and no other phases were detected. Despite a relatively low temperature (130°C) and a short time (20 minutes) of synthesis, the X-ray peaks demonstrate a relatively high intensity revealing a good crystallinity of the obtained particles. Both, structure and crystallinity, are consistent with similar studies carried out in comparable conditions[22,25]. The peak widths suggest that the product powders have a nanocrystalline nature. By applying Debye-Sherrer formula to the first peak at 16° corresponding to the reflection (020), the crystal size of the obtained samples was found to be in the range of 4-6 nm. This size variation is not significant indicating that only a slight change in crystallite size is observed in the corresponding diffracted direction (020). In the XRD pattern of the sample synthesized at the lowest concentration (0.025 mol/L) the peak at 24° indexed as (120) clearly appears, whereas it is almost not visible for the samples obtained at higher concentrations.

The SEM observation reveals that the obtained nanoparticles have a platelet shape (Figure 3). This specific morphology reflects the anisotropic structure of tungstite and is in agreement with previous reports[21,22,24]. The results of the measurements of the particle size and size distribution are summarized in Table 1. According to SEM and DLS, the particle size decreases with an increase in metal salt concentration. This trend is spectacular at the lowest concentration (0.025 M) where the lateral size of the platelets, as found by SEM, is 250 nm. However, the thickness (5-10 nm) does not change with the decrease of the salt concentration. Therefore, particles obtained at higher concentrations demonstrate a lower aspect ratio in comparison with those synthesized at C = 0.025 mol/L. Similar trend was observed for tungstite synthesis at 145°C[22].

Table 1. Particle size measured by SEM and DLS.

WCl_6 concentration mol/L	Size by SEM nm	D_h by DLS nm
0.025	250 ± 30	550
0.05	40 ± 7	140
0.10	30 ± 5	100
0.15	30 ± 6	100

In order to explain such a drastic change in the particle size, the particle growth mechanism should be looked into. Reactions involving the formation of a solid can be divided into two steps: the first step of nucleation and growth and the second step where only growth occurs. For the former, thermodynamic studies have established that the nucleation rate strongly depends on the concentration of the solid precursor[26].

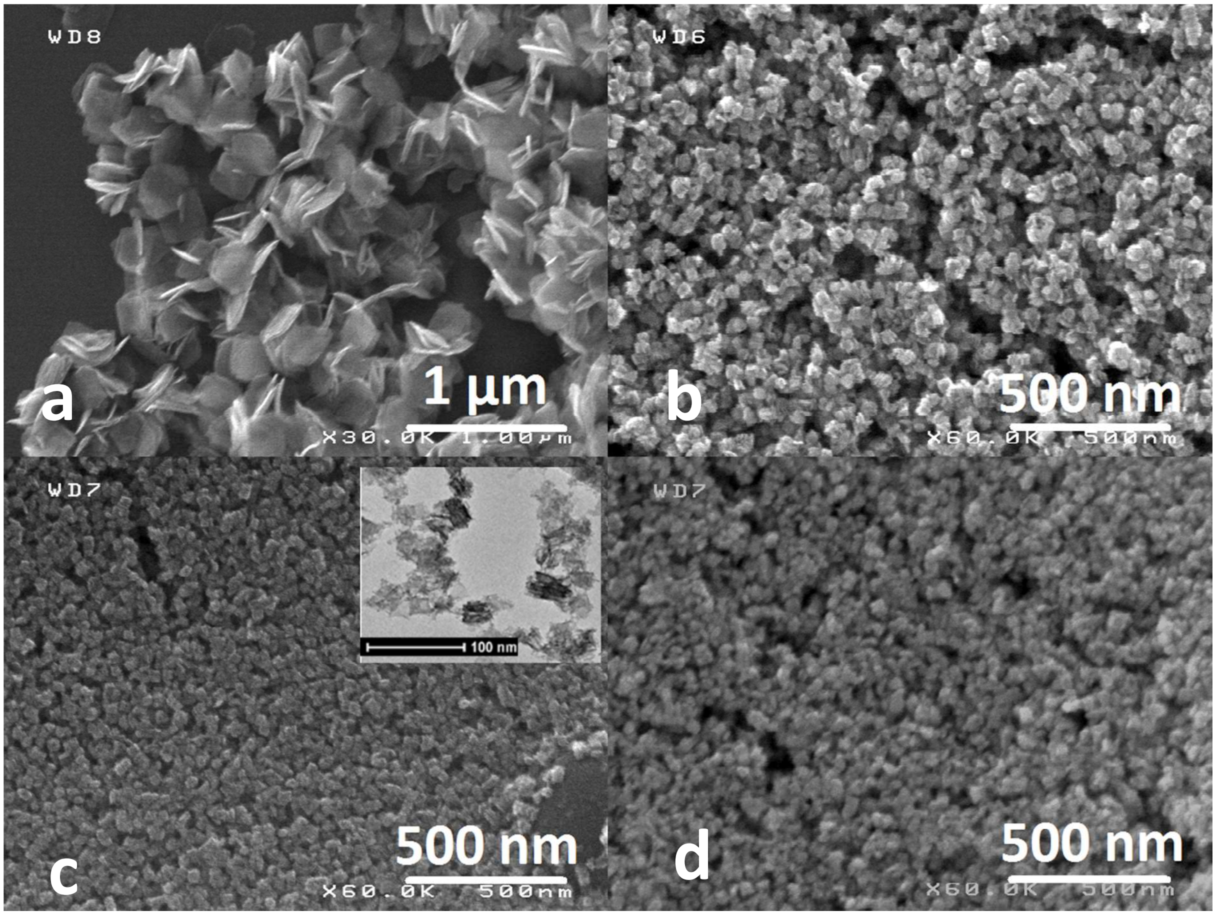

Figure 3. SEM images of tungstite particles obtained at different concentrations: 0.025 mol/L (a), 0.05 mol/L (b), 0.10 mol/L (c) and 0.15 mol/L (d). In the inset: a HTEM image.

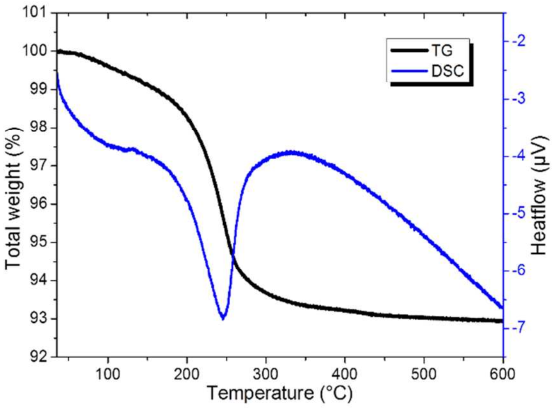

Figure 4. TG-DSC analysis of tungstite nanoparticles obtained at concentration 0.10 mol/L.

Thus, at higher concentrations, an instant nucleation prevails over the growth and leads to a greater number of smaller nanoparticles. At the lowest concentration, the growth step is predominant. Moreover, since tungstite preferentially growths in the directions perpendicular to the axe [010], these factors explain the high aspect ratio for particles obtained at 0.025 mol/L. This underlines the importance of controlling the nucleation step (in our study, through concentration) in the process of producing small and narrow-sized nanoparticles. From this point of view, the microwave-assisted heating is advantageous. Firstly, it allows a rapid heating rate that quickly triggers the nucleation. Secondly, microwaves instantly propagate in the whole sample resulting in a homogeneous heating with almost no temperature gradient and, thus, additionally diminishing the particle size variation.

TG-DSC analysis allowed to found the water content as well as to control the presence of a possible organic contamination in the obtained powders (Figure 4). The first weight loss (about 1%) is accompanied with a weak endothermic effect and occurs between 100°C and 180°C. It corresponds to desorption of water and solvent molecules from the particle surface[27]. This loss is directly followed by a greater weight loss coupled with an endothermic effect peaked at 245°C. This step can be attributed to the removal of the strongly bound water and the transformation of $WO_3 \cdot H_2O$ into anhydrous WO_3[27]. The observed total weight loss of 7% is very close to the theoretical one (7.2%) indicating also that a possible contamination by organic by-products or solvent that is observed for convenient heating[22] is negligible. From this point of view, the application of a rapid microwave-assisted heating is advantageous as it allows a reduction of contamination that can deteriorate the properties of the final HTL film.

3.2 Particles dispersion and films formation

Charge transport layers based on transition metal oxides and used in organic solar cells, in general, exhibit a high electrical resistivity, that is why the thickness of a transporting layer rarely exceeds 50-100 nm. To be able to form such a thin film, it is essential to handle particles of smaller sizes. A narrow size distribution is also a critical issue as it can impact thickness reproducibility and roughness of the resulted film.

Since the stability of the colloidal dispersion is a key point to the formation of thin and homogeneous films, an additional study was performed. It turned out that the obtained nanoparticles were not stable in pure (absolute) ethanol and rapidly flocculated. It was found that when the particles were dispersed in an ethanol solution containing a small amount of water (0.5 % by volume), the nanoparticle colloid remained stable for several weeks. It is believed that water molecules stabilize the nanoparticles by increasing the electrostatic charges at the surface. The DLS measurements (Figure 5) show that the distribution of the hydrodynamic diameters has only a single narrow peak, suggesting that no aggregation occurred in the solution. Moreover, the measured value of the zeta-potential of the colloid in the water-ethanol mixture was found to be -35± 10 mV indicating a good electrostatic stability due to repulsions between the nanoparticles. The DLS measurements give particle sizes almost twice bigger than those observed by SEM. In fact, it is not surprising because the former method describes hydrodynamic diameters of scattering centers surrounded by solvated spheres.

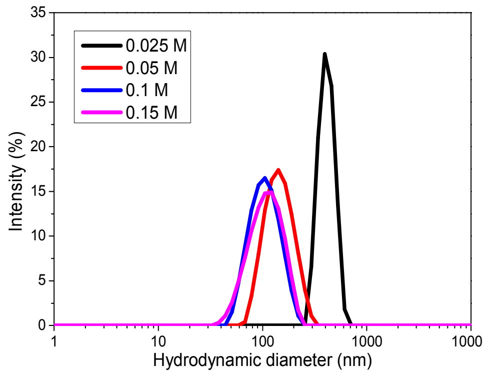

Figure 5. DLS measurements of ethanolic colloids with tungstite nanoparticles synthesized at different concentrations.

For further studies, the particles with the sizes of 30 nm were chosen. As it will be shown below, these particles allow a good tailoring of the thickness and a relatively low roughness. The stabilized tungstite nanoparticle dispersion was spin-coated in air to form a thin film on a glass/ITO substrate. The AFM images (Figure 6, right) clearly show that the film is composed of homogeneously deposited nanoparticles. Compared to the bare ITO surface (Figure 6, left), the roughness has slightly increased from 2 nm to 7 nm (see also Table 2). The latter value is consistent with prior studies on nanoparticles used for film preparation[6,11] and is considered to be good enough for further deposition of the 200 nm thick active layer. In a standard experiment, the HTL film thickness was 40 nm.

To allow a better charge transport from the active layer to the electrode, the intermediate charge transporting layer must provide suitable energy level alignment with the adjacent layers. The work function values of the considered materials are presented in Table 2. The $WO_3 \cdot H_2O$ film exhibits a work function of 5.0 eV. Hydrated form does not seem to significantly alter the work function. Higher work function values have been reported elsewhere: Stubhan et al [11] found a work function of 120 nm films of WO_3 to be 5.35 eV while Meyer et al obtained a close value of 5.4 eV for WO_3 films after air exposure[28]. But values around 5.0 and less have been reported in the literature: Guillain et al obtained 4.7 eV for solution processed films[19] and Lee et al found work functions to be from 5.03 to 5.17 eV depending of the annealing temperature of WO_3 films prepared by thermal evaporation[12]. Various elaboration procedures thus seem to lead to a significant spread in the data. In this respect our value of 5.0 eV appears fully reasonable. Besides, since the work-function value found for bare ITO is 4.7 eV and HOMO of P3HT is known to be close to 5.1 eV, it is intermediate and should provide a good hole transport from the active layer to the ITO electrode.

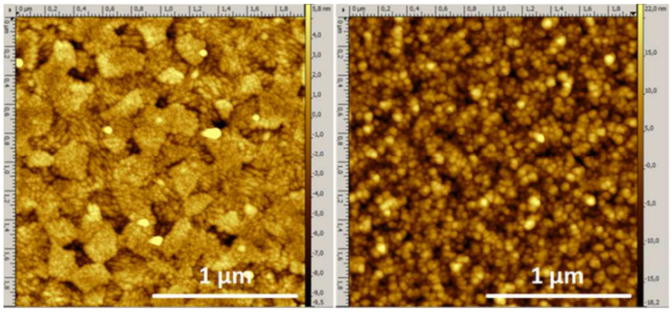

Figure 6. AFM images of bare ITO substrate (left) and a tungstite film deposited on ITO (right).

Table 2. Work function obtained by KPFM and roughness calculated from AFM images.

	ITO	$WO_3 \cdot H_2O$	PEDOT:PSS	P3HT
work function or HOMO level, eV	4.7	5.0	5.1*	5.1*
roughness (RMS), nm	2.3	7.0	-	-

* - values taken from the literature or provided by the product supplier

3.3 Photovoltaic properties

A comparative study of standard structure solar cells with tungstite nanoparticles or PEDOT:PSS as hole transporting layer was carried out. The curves of the current-voltage

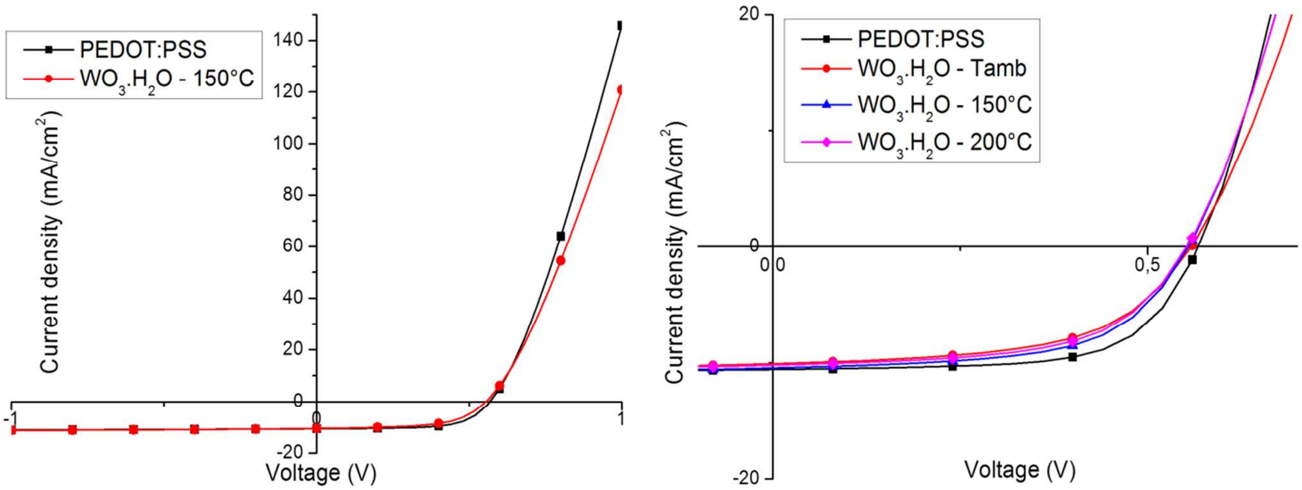

Figure 7. Comparison of current-voltage characteristics of polymer solar cells with HTL on the base of tungstite nanoparticles (circle, up triangle, down triangle) and PEDOT:PSS (square).

Table 3. Photovoltaic characteristics of solar cells with HTL on the base of tungstite nanoparticles and PEDOT:PSS annealed at different temperatures in air for 30 min. The error intervals correspond to standard deviation.

HTL	Annealing Temperature (°C)	V_{oc} (mV)	J_{sc} (mA/cm^2)	FF (%)	PCE (%)	R_s (Ω)	R_{sh} (kΩ)	Best PCE	Number of cells
PEDOT:PSS	180 °C	566 ± 3	10.4 ± 0.3	64 ± 1	3.8 ± 0.1	10 ± 1	9 ± 1	3.92	6
$WO_3·H_2O$	Ambient	558 ± 4	9.7 ± 0.4	57 ± 1	3.1 ± 0.1	12 ± 1	5 ± 4	3.20	5
	150 °C	555 ± 7	10.0 ± 0.5	58 ± 1	3.2 ± 0.2	12 ± 1	6 ± 4	3.49	6
	200 °C	552 ± 9	9.5 ± 0.5	57 ± 1	3.0 ± 0.2	12 ± 1	4 ± 3	3.28	4

characterization are shown in Figure 7. The photovoltaic parameters calculated from the curves are summarized in Table 3. The values were obtained by averaging the results from 4 - 6 cells. The best PCE value for each experimental condition is given.

The best devices with $WO_3·H_2O$ (T=150°C in Table 3) exhibit an average power conversion efficiency (PCE) of 3.2% with the best cell at 3.49%. Devices fabricated with PEDOT:PSS give better PCE: 3.8% in average and 3.92% for the best cell. Concerning V_{oc}, no significant difference is seen between PEDOT:PSS and tungstite incorporating devices However the J_{sc} and FF are slightly lower, compared to the reference cells. The J_{sc} reduction means that fewer charges are collected at the electrode. This could be explained by recombination at interfaces between two layers (active layer/tungstite or tungstite/ITO). A 10% decrease of the FF is observed in devices with $WO_3·H_2O$ as HTL. Such a decrease can generally be attributed to a degradation of either the series resistance (R_s) or the shunt resistance (R_{sh}). In the present work, it is believed that the contact between tungstite and the active layer is responsible for the increase of series resistance which is clearly visible in Figure 7. Indeed, with PEDOT:PSS as HTL, the polymer has a low surface roughness around 1 nm[9,16], whereas the nanoparticle layer has a 7 nm roughness (Table 2), decreasing the quality of the contact and, therefore, increasing the contact resistance. In addition, the increased surface roughness can be invoked to account for the decrease in J_{sc} as it amounts to a higher specific surface with an increased number of dangling bonds and potential chemical contamination. The decrease of the shunt resistance (see Table 3) can be attributed to the low thickness of the layer, allowing some partial direct contacts between the electrode and the active layer. With P3HT:PCBM active polymers and tungsten oxide deposited by solution-processed methods in standard structure, similar results can be found in the literature. Choi et al.[10] obtained a PCE of 3.4% with WO_3 from a sol-gel process compared to 3.8% with PEDOT:PSS as HTL. With milled WO_3 nanoparticles, Huang et al.[29] obtained a 3.2% photovoltaic efficiency (3.9% for their reference cells with PEDOT:PSS). Stubhan et al.[11] obtained 3.2% for both PEDOT:PSS and WO_3 nanoparticles. In these reports, the J_{sc} and the FF are lower for tungsten oxide compared to PEDOT:PSS, which is consistent with our results.

Short time and low temperature of treatment are normally required for methods compatible with flexible substrates and applicable in industrial processes such as roll-to-roll. From this point of view, it was interesting to investigate the effect of annealing temperature. To compare with the results obtained at 150°C, two additional series of cells were prepared and treated in air at ambient temperature and 200°C. It was found that, regardless the annealing temperature, their power conversion efficiencies are almost the same with an average value between 3.0% and 3.2% (Table 3). These results show that the films deposited from a nanoparticle dispersion do not require a conversion treatment as most of the sol-gel processes do. Moreover, this nanoparticle approach is compatible with flexible substrates such as polyethylene terephthalate (PET), which usually does not allow annealing temperatures above 140°C.

As a comparison, in a sol-gel process reported by Choi *et al*[10], an overnight hydrolysis of tungsten ethoxide was needed to complete the material conversion. The PCE was varied between 0.33% and 3.37% depending on the HTL thickness. In another sol-gel deposition of WO_3 from tungsten isopropoxide an efficiency of 4.33% was obtained after annealing at 150°C[18]. To achieve a functional HTL, these sol-gel methods require a relatively high temperature or a long time of conversion that is not always compatible with industrial processes.

Conclusions

The simple microwave-assisted synthesis described here provides a low cost production of $WO_3 \cdot H_2O$ nanoparticles with a very low organic contamination. It has been shown that their size can be tuned by varying the precursor salt concentration in the solution. A fast nucleation rate at high concentration gives rise to particles with smaller size. The deposition of 30 nm platelet-like particles dispersed in ethanol solution led to homogeneous and thin films with a work function of 5.0 eV, providing a suitable energy level alignment. Devices incorporating tungstite nanoparticles as hole transporting layer have exhibited good photovoltaic performances (PCE up to 3.49%). Compared with PEDOT:PSS devices, a slight decrease in J_{sc} and FF was observed. Also, it has been shown that an annealing treatment was not required to achieve a full transformation toward a functionalized layer. In organic solar cells with inverted structure, where the HTL is deposited on the active layer, annealing temperature is limited by the thermal stability of the active layer materials. From this point of view, this nanoparticle approach could be of interest. Finally, this technique could also be applied to flexible substrates and the formation of films through a nanoparticle solution has been shown to be compatible with industrial processes. Regarding perspectives, stability should also be studied in order to investigate the effect of the inorganic interlayer.

Acknowledgements

This work has been funded by the French agency ANRT (Agence Nationale de la Recherche Technologique), PCAS and the CEA. The AFM-KPFM measurements were performed at the CEA Minatec Nanocharacterization Platform (PFNC).

References

1. M. A. Green, K. Emery, Y. Hishikawa, W. Warta and E. D. Dunlop, *Prog. Photovolt. Res. Appl.*, 2014, **22**, 1–9.
2. M. P. de Jong, L. J. van Ijzendoorn and M. J. A. de Voigt, *Appl. Phys. Lett.*, 2000, **77**, 2255.
3. P. Qin, G. Fang, N. Sun, X. Fan, Q. Zheng, F. Chen, J. Wan and X. Zhao, *Thin Solid Films*, 2011, **519**, 4334–4341.
4. A. K. K. Kyaw, X. W. Sun, C. Y. Jiang, G. Q. Lo, D. W. Zhao and D. L. Kwong, *Appl. Phys. Lett.*, 2008, **93**, 221107.
5. S. R. Hammond, J. Meyer, N. E. Widjonarko, P. F. Ndione, A. K. Sigdel, A. Garcia, A. Miedaner, M. T. Lloyd, A. Kahn, D. S. Ginley, J. J. Berry and D. C. Olson, *J. Mater. Chem.*, 2012, **22**, 3249.
6. J. Meyer, R. Khalandovsky, P. Görrn and A. Kahn, *Adv. Mater.*, 2010, **23**, 70–73.
7. M. D. Irwin, D. B. Buchholz, A. W. Hains, R. P. H. Chang and T. J. Marks, *Proc. Natl. Acad. Sci.*, 2008, **105**, 2783–2787.
8. K. X. Steirer, J. P. Chesin, N. E. Widjonarko, J. J. Berry, A. Miedaner, D. S. Ginley and D. C. Olson, *Org. Electron.*, 2010, **11**, 1414–1418.
9. S. Han, W. S. Shin, M. Seo, D. Gupta, S.-J. Moon and S. Yoo, *Org. Electron.*, 2009, **10**, 791–797.
10. H. Choi, B. Kim, M. J. Ko, D.-K. Lee, H. Kim, S. H. Kim and K. Kim, *Org. Electron.*, 2012, **13**, 959–968.
11. T. Stubhan, N. Li, N. A. Luechinger, S. C. Halim, G. J. Matt and C. J. Brabec, *Adv. Energy Mater.*, 2012, **2**, 1433–1438.
12. S. B. Lee, J. Ho Beak, B. hyun Kang, K.-Y. Dong, Y.-Y. Yu, Y. Doo Lee and B.-K. Ju, *Sol. Energy Mater. Sol. Cells*, 2013, **117**, 203–208.
13. J.-S. Huang, C.-Y. Chou, M.-Y. Liu, K.-H. Tsai, W.-H. Lin and C.-F. Lin, *Org. Electron.*, 2009, **10**, 1060–1065.
14. K. Zilberberg, S. Trost, H. Schmidt and T. Riedl, *Adv. Energy Mater.*, 2011, **1**, 377–381.
15. G. Terán-Escobar, J. Pampel, J. M. Caicedo and M. Lira-Cantú, *Energy Environ. Sci.*, 2013, **6**, 3088.
16. F. Xie, W. C. H. Choy, C. Wang, X. Li, S. Zhang and J. Hou, *Adv. Mater.*, 2013, **25**, 2051–2055.
17. A. Soultati, A. M. Douvas, D. G. Georgiadou, L. C. Palilis, T. Bein, J. M. Feckl, S. Gardelis, M. Fakis, S. Kennou, P. Falaras, T. Stergiopoulos, N. A. Stathopoulos, D. Davazoglou, P. Argitis and M. Vasilopoulou, *Adv. Energy Mater.*, 2014, **4**, n/a–n/a.
18. Z. Tan, L. Li, C. Cui, Y. Ding, Q. Xu, S. Li, D. Qian and Y. Li, *J. Phys. Chem. C*, 2012, **116**, 18626–18632.
19. F. Guillain, D. Tsikritzis, G. Skoulatakis, S. Kennou, G. Wantz and L. Vignau, *Sol. Energy Mater. Sol. Cells*, 2014, **122**, 251–256.
20. WO 2013/059948 Al, 2013.
21. M. Niederberger, M. H. Bartl and G. D. Stucky, *J. Am. Chem. Soc.*, 2002, **124**, 13642–13643.
22. N. Le Houx, G. Pourroy, F. Camerel, M. Comet and D. Spitzer, *J Phys Chem C*, 2009, **114**, 155–161.
23. A. Karpinski, S. Berson, H. Terrisse, M. Mancini-Le Granvalet, S. Guillerez, L. Brohan and M. Richard-Plouet, *Sol. Energy Mater. Sol. Cells*, 2013, **116**, 27–33.
24. I. Olliges-Stadler, J. Stötzel, D. Koziej, M. D. Rossell, J.-D. Grunwaldt, M. Nachtegaal, R. Frahm and M. Niederberger, *Chem. – Eur. J.*, 2012, **18**, 2305–2312.
25. I. Olliges-Stadler, M. D. Rossell, M. J. Süess, B. Ludi, O. Bunk, J. S. Pedersen, H. Birkedal and M. Niederberger, *Nanoscale*, 2013, **5**, 8517.
26. G. Cao, *Nanostructures & nanomaterials: synthesis, properties, and applications*, World Scientific, New Jersey, 2nd ed., 2011.
27. Y. Liu, Q. Li, S. Gao and J. K. Shang, *CrystEngComm*, 2014, **16**, 7493.

28. J. Meyer, S. Hamwi, T. Bülow, H.-H. Johannes, T. Riedl and W. Kowalsky, *Appl. Phys. Lett.*, 2007, **91**, 113506.
29. J.-H. Huang, T.-Y. Huang, H.-Y. Wei, K.-C. Ho and C.-W. Chu, *RSC Adv.*, 2012, **2**, 7487.